Progress In Electromagnetics Research, Vol. 164, 97–107, 2019

Internal Magnetic Induction Tomography Using a Single Coil

Joe R. Feldkamp* **and Stephen Quirk**

Abstract—Most imaging modalities image an object's interior while all instrumentation, including sources and receivers, is externally located. One notable exception is ultra-sound (US), which can be miniaturized sufficiently to locate a US transducer within an object and gather data for image reconstruction. Another is cross-borehole geophysical imaging. The goal of any internal imaging modality is to provide images of greater fidelity while avoiding interfering structures. Due to the bulkiness of multi-coil magnetic induction tomography (MIT), transmitting and receiving coils are never placed within small targets (e.g., a human body). Here, we demonstrate a novel implementation of *single-coil* MIT that performs a scan all while the coil is located within the interior of a small, lab-created phantom consisting of salt-doped agarose. Phantom geometry is annular, consisting of a 6.0 cm diameter channel of depth 5.5 cm surrounded by a 3.0 cm thick cylindrical wall. An embedded, centrally located agarose gel annulus, 2.0 cm thick, is doped with sufficient NaCl to elevate its conductivity above that of surrounding agarose. The resulting nearly axisymmetric phantoms consist of material having conductivity ranging from 0.11 to 10.55 S/m. A scan is accomplished robotically, with the coil stub-mounted on the positioning head of a 3-axis controller that positions the planar circular loop coil into 360 or 720 preset internal positions. Image reconstruction from gathered data is shown to correctly reveal the location, size and conductivity of the approximately axisymmetric inclusion.

1. INTRODUCTION

An image of the electrical *small* conductivity distribution, obtained from either electrical impedance tomography (EIT) [1, 2] or magnetic induction tomography (MIT) [3–6], can be useful in both medical and geological applications. In medicine, a goal of imaging is to differentiate and identify either normal or abnormal tissues [7], while in geology, imaging can be useful for resource discovery [8]. Except for geological applications, MIT has only been implemented by locating a system of coils in the immediate vicinity of a conductive target, with any one of the externally positioned coils receiving excitation while all others exhibit a response that is influenced by the intervening target [9]. A variety of methods are then used for image reconstruction, with resolution dependent upon methods used [10], and nonlinear methods usually required in multi-coil MIT [11].

A relatively recent MIT advance has shown that reconstruction of electrical conductivity images is feasible by scanning in the vicinity of a target with just a single coil consisting of concentric circular loops [12] — scanning refers to the repeated repositioning of a coil in a target's vicinity while measuring a suitable coil property. Loops may lie in multiple planes provided that the gap between layers is very small compared to loop radii [13]. The single-coil approach is based upon a closed-form analytical formula that relates coil ohmic loss to coil orientation and position relative to an arbitrary 3D conductivity distribution. Because the analytical result was obtained through perturbative solution of Maxwell's equations, the first-order accurate formula only fully captures skin-effects for relatively low-conductivity materials — ~ 400 S/m or less [14]. But this is certainly adequate for a number of interesting biological

Received 4 December 2018, Accepted 14 February 2019, Scheduled 6 March 2019
* Corresponding author: Joe R. Feldkamp (jrfeldcinci@gmail.com).
The authors are with the Kimberly-Clark Corp., Roswell, GA, USA.

and geological materials [15–17]. Furthermore, the formula permits the straightforward use of linear reconstruction methods [18]. We note that other analytical strategies have recently been devised for determining the interaction of electrically small loop antennas with heterogeneous conductive structures — in particular, the work of Parise [19] considers a small loop antenna in the immediate vicinity of a plane-layered structure.

Because our approach is accomplished with just a single coil, the possibility exists of placing a sufficiently small coil within the interior of a target to enable "internal scanning", provided there are entrance points that allow insertion of a small coil. Biological examples could include the esophagus and lower gastrointestinal tract, while geological examples would include investigational boreholes. In many instances, especially in geological situations, the material along the length of a nearly cylindrical interior passageway has an electrical conductivity distribution that is approximately axisymmetric. If so, image reconstruction could be simplified to either one or two dimensions, if full 3D detail is not needed. However, severely non-axisymmetric conditions will require 3D reconstruction and are likely more challenging, since induced eddy currents which circulate around a cylindrical passageway may be forced to pass through both low and high conductivity regions — a situation that can greatly limit current flow, and hence the measured ohmic loss.

Rather than attempt an "internal scan" on a phantom having a complicated 3D electrical conductivity distribution, phantoms are built that are intended to be axisymmetric. These are annular in shape, with a cylindrical passageway that affords enough clearance to support an internal scan using a small coil — 5.0 cm diameter in this work. Coil positioning is accomplished with a 3-axis controller that places the coil's center at some number of preselected locations, all while keeping the coil plane perpendicular to the phantom's annular axis. Acquired coil loss values, together with corresponding coil-center positions, are processed with a full 3D image reconstruction algorithm. Full 3D reconstruction is necessary since our methods for phantom construction, using NaCl-doped agarose, are only able to produce phantoms having approximate axisymmetric structure. A number of examples are given that vary the conductivity of an embedded annular ring and surrounding matrix material. Ongoing research is planned for smaller coils and strongly non-axisymmetric phantoms.

2. IMAGE RECONSTRUCTION VIA CONVOLUTION INTEGRAL INVERSION

Coil geometry is circular, consisting of four 5.0 cm diameter concentric loops spaced just 0.3 mm apart on a four-layer PCB (printed circuit board). The 2.0 oz Cu traces are connected in series [12] to produce an inductance of 2.36 μH. For the circular coil type used here, inductive coil loss can be written as a convolution of conductivity, $\sigma(\vec{r})$, and kernel $G(\vec{r}_c)$ [13, 18]:

$$Z(\vec{c}) \;=\; \int \sigma\left(\vec{r}\right) G\left(\tilde{R}^T\left(\vec{r}-\vec{c}\right)\right) dxdydz \tag{1}$$

Integration is over all space. The kernel is related to details of coil construction, as well as coil position and orientation relative to a conductive target:

$$G\left(\vec{r}_c\right) = \frac{\mu^2\omega^2}{4\rho\pi^2} \sum_{j,k} \sqrt{\rho_j \rho_k}\; Q_{1/2}\left(\eta_j\right) Q_{1/2}\left(\eta_k\right) \tag{2}$$

Arguments for the circularly symmetric ring (or toroid) function $Q_{1/2}$ (see Appendix A for explicit form) lie in the interval $1 < \eta < \infty$ [20] and are related to field position by:

$$\eta_j = \frac{\rho^2 + \rho_j^2 + z_c^2}{2\rho\rho_j} \tag{3}$$

Using any suitable fixed laboratory coordinate system, other symbols in Equations (1-3) are defined by:

$\sigma(\vec{r})$: *Electrical conductivity (real part) at field position:* $\vec{r} = (x, y, z)$

ρ_j: *Cylindrical radial distance from coil axis to wire loop 'j'*

ρ: *Cylindrical radial distance from coil axis to field point*

$z_c = z_\perp$: *Perpendicular distance from coil plane to field point.*

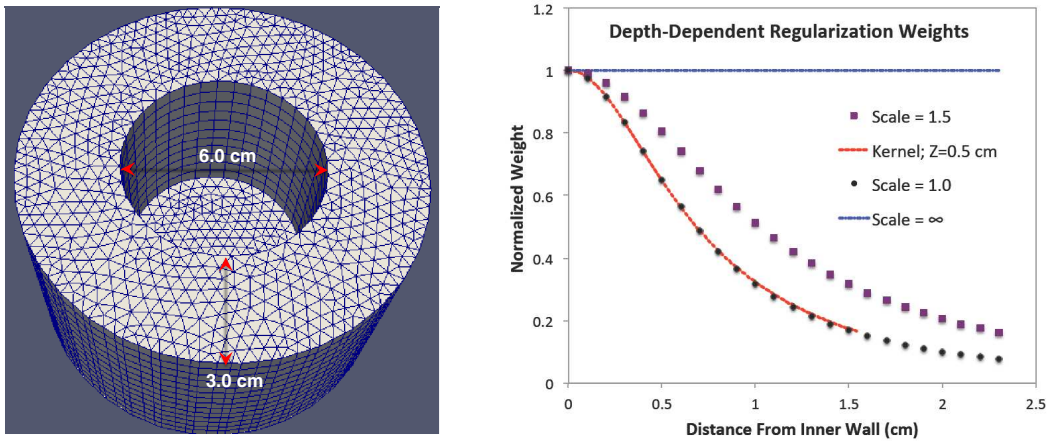

(a) (b)

Figure 1. (a) Finite element mesh consisting of 18,832 prismatic elements — annulus hole is 5.5 cm deep. Phantom base (stage) is 1.5 cm thick; (b) Regularization weights used for image reconstruction — '∞' corresponds to $\tilde{D} = \tilde{I}$. Parameter *scale* = 1.5 cm was used throughout.

μ: *Magnetic permeability — considered uniform*

ω: *Angular frequency*

Vector $\vec{c}$ connects the origin of the chosen fixed laboratory reference frame (usually origin of a finite element mesh frame) with the coil's center, while the vector $\vec{r}_c$ extends from the coil center to field point, in the coil reference frame. In this application, the rotation matrix $\tilde{R}$ is just the identity matrix, since the coil plane is maintained parallel to the XY plane of the finite element mesh of the phantom. After discretizing the convolution integral using deformed prismatic finite elements [21] ($\sim 18,832$ elements — Figure 1(a)), a system of equations is produced that predicts coil loss $\vec{Z}$ at the set of preselected coil positions. A non-negative least squares problem is set up and regularized via penalty matrix $\tilde{D}$:

$$\min \ \frac{1}{2}\left\|\tilde{A}\vec{\sigma} - \vec{Z}\right\|_2^2 + \frac{1}{2}\tau^2\left\|\tilde{D}\left(\vec{\sigma} - \vec{\sigma}_{avg}\right)\right\|_2^2 \quad s.t. \quad \vec{\sigma} \geq 0 \tag{4}$$

After converting minimization problem in Eq. (4) to standard form [22, 23], image reconstruction proceeds via singular value decomposition (SVD) of the matrix $\tilde{A}\tilde{D}^{-1}$. Solution non-negativity is enforced through application of KKT (Karush-Kuhn-Tucker) multipliers and active set technology [18]. The global regularization parameter is found by stepping τ through the singular values produced by the SVD, from largest to smallest. The process is stopped when the solution error norm approaches the inductive loss vector error norm from above — known as the discrepancy principle [23]. Up to five iterations are usually needed for each singular value tested in order to satisfy KKT conditions. Though image reconstruction benefits from knowing the a priori position of the inner and outer phantom boundaries, the conductivity, size and vertical location of the embedded higher conductivity inclusion are unknown.

Because the kernel decreases with radial distance into the annular specimen, the diagonal regularization matrix $\tilde{D}$ is set up to apply a smaller penalty at nodes located more radially distant from the coil edge, mirroring the kernel itself. Figure 1(b) illustrates how the convolution kernel decays radially outside of the 2.5 cm coil radius, indicating that regions farther from the coil contribute less to the predicted inductive loss. Since noise and drift are inevitable in any instrumentation, reconstruction of the electrical conductivity at locations more distant from the coil becomes difficult due to decaying kernel behavior. A way to partially mitigate this problem is to reduce the penalty imposed at mesh nodes located more deeply into the target [24]. To set the diagonal elements of $\tilde{D}$, $\{d_j\}$, we use an approximation for the radial decrease in the convolution kernel outside of the coil's largest loop (2.5 cm

radius):

$$d_j = \frac{\exp(-\lambda_1 \rho_j / scale)}{1 + \lambda_2 (\rho_j / scale)^2} \tag{5}$$

For all image reconstructions, parameters λ_1 and λ_2 are set to 0.05 and 2.0, respectively, while the parameter $scale = 1.5\,\text{cm}$. If $scale = 1.0\,\text{cm}$, then the depth-dependent regularization weights applied at radial depth ρ_j follow kernel decay behavior almost exactly at $z_\perp = 0.5\,\text{cm}$ away from the coil plane, as Figure 1(b) shows — note that other choices for $z_\perp$ are possible for this illustration of kernel behavior. Equation (5) allows considerable flexibility in fine-tuning image reconstruction — setting $scale = \infty$ weights all locations ρ_j equally, but tends to cause an exaggerated electrical conductivity distribution near the inner annular wall; on the other hand, setting $scale = 1.0\,\text{cm}$ penalizes near locations more strongly, leading to an exaggerated conductivity farther from the annular inner wall; however, $scale = 1.5\,\text{cm}$ provides a reasonable compromise, which is half the annular wall thickness, so is used throughout.

Solution of minimization problem in Eq. (4) is discussed at length in a recent publication [18], including the procedure for computing $\vec{\sigma}_{avg}$. To facilitate image comparison, an identical black-body color scheme is used throughout — Black (0 S/m); Red (one third full scale); Yellow(two thirds full scale); and, White (full scale), with 256 gradations across the spectrum.

3. INDUCTIVE LOSS MEASUREMENT

Coil geometry and construction follows that described previously [12–14] — here, four planes of concentric circular loops are spaced 0.3 mm and prepared on a four layer PCB. Loop traces are 0.5 mm wide, built from 2 oz. copper with radius equal to 2.5 cm, all wired in series, giving four loops total. There is a 1 mm buildup of PCB material on the side of the coil facing outward, so that there is at least a 1 mm separation between coil and mesh floor which envelops the 3-axis platform beneath the phantom. Coil inductance, L, is calculated from equations given in earlier work [13] — repeated here in terms of loop self-inductance, L_{sj}, and mutual inductances between loops, M_{jk}:

$$L = N_{layers}^2 \left(\sum_{j=1}^{5} L_{sj} + \sum_{j,k=1}^{5} M_{jk} \right) \quad ; \quad j \neq k \tag{6}$$

Since there are four layers in the present work, a factor of 16 multiplies each sum. Equation (6) is a reasonable approximation for our coil's inductance provided that the distance between layers is very small compared with loop radii. Inductance for our coil was calculated to be 2.355 μH, which is used in all computations here and agrees with measurement to within 1% [12].

Starting from a model of a real inductor that consists of an ideal inductor in series with an ideal 'lossy' resistor, and then placed in parallel with an ideal capacitor, coil loss is computed from a measured change in the real part of admittance, δY_{re}, relative to the free space value, which subtracts the effect of any loss intrinsic to the coil. Given inductance L and frequency ω, coil loss is computed from the formula [12]:

$$\delta Z = \omega^2 L^2 \delta Y_{re} \tag{7}$$

Thus, two admittance measurements are needed — one in free space that minimizes interaction with nearby conductive objects, and then subsequent measurements in the immediate vicinity of a conductive specimen. When making 20 to 30 free space measurements at 12.5 MHz, admittance standard deviation is typically $\sim 0.11\,\mu\text{S}$ out of $\sim 100.0\,\mu\text{S}$. Additional details are found in [26].

4. THREE-AXIS COIL POSITIONING IN THE VICINITY OF AGAROSE PHANTOMS

Previously, we have used optical means to track the position and orientation of our planar coils [26, 27], which has been useful for performing free-form hand scans. Here, because of the restricted space available for a coil introduced into an open channel not much larger than the coil itself, we have chosen

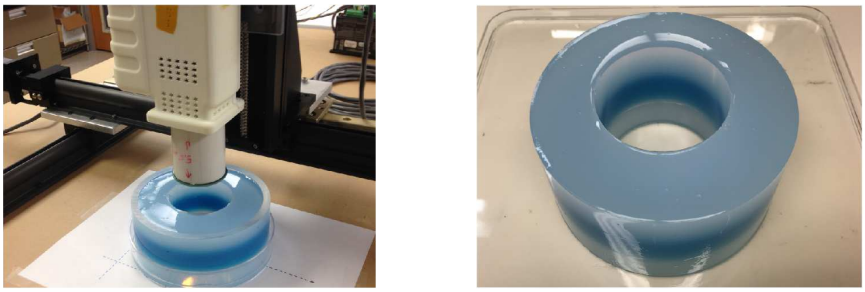

(a) (b)

Figure 2. (a) Agarose phantom resting on the positioning stage, just beneath a stub-mounted 5.0 cm diameter coil, which is relocated by the 3-axis controller affixed to the same stage; (b) Close up view of the annular phantom and its central cavity — the blue, 2.0 cm thick embedded annular inclusion is doped with NaCl, elevating its "uniform" conductivity above surrounding agarose.

to use a 3-axis positioning system consisting of linear slides driven by stepper motors set to provide one rotation in 2000 steps. The resulting positioning precision along any of the three axes is ± 0.0635 mm. Overall positioning accuracy is limited by a required initial alignment of both the coil and phantom over the stage, which involves a centering step guided by cross-hairs etched into the stage, so that positioning accuracy is $\sim \pm 0.25$ mm. Figure 2(a) shows the phantom positioned just beneath the coil, mounted on a stub which is attached to the electronics enclosure. Figure 2(b) shows the phantom removed from its support or retaining ring, which was helpful in maintaining its stability during a scan.

Scans are accomplished by simultaneously reading a value of inductive loss and the corresponding position, as determined from a file containing the set of preset coil locations. At each position, 10 values of inductive loss are acquired and averaged to help with noise reduction. These averages are obtained at either 360 or 720 positions in the vicinity of the phantom axis while the coil is inside the annulus. Scanning proceeds at a rate of ~ 2 new positions per second, with 0.25 s needed to acquire the 10 loss values at a particular location. To cope with drift, the coil is periodically removed from the annulus interior for a free space measurement to aid baseline tracking, which is done after every ~ 150 measurements. Video of a partial scan is posted online: *Click-Here*

Agarose phantoms were prepared as previously described [25] — without NaCl doping, agarose conductivity is ~ 0.11 S/m; conductivity is ~ 2.11 S/m if doped with 2.4% w/v, and ~ 10.55 S/m if doped at 12.0% w/v. The annular inclusion (dyed blue) is always ~ 2.0 cm thick and centered at ~ 4.25 cm in the *mesh frame*. Our construction methods intended to create annular inclusions with uniform conductivity across both thickness and radial dimensions. However, results will show that perfect uniformity within an inclusion is not likely obtained.

Sampling locations for either of the sampling sets, 360 or 720, are shown in Figure 3. In either case, there are 30 sampling layers spaced 2.0 mm apart — 12 per sampling horizon for the set of 360, and 24 per sampling horizon for the set of 720. A "sampling disk" having 3.0 mm radius is shown to aid comparison between the two sets — the specified region limits coil center positioning to avoid coil-phantom contact. If the coil, which has radius 25.0 mm, were centered on the boundary of the sampling disk, then the coil's PCB traces would be just 2.0 mm away from the inner wall of the phantom which itself has a radius of 30.0 mm. So clearly, the 720 set approaches the phantom wall more closely, but still uses the same lattice structure.

5. IMAGE RECONSTRUCTION RESULTS

Three phantoms were constructed: 0.11 S/m background (no NaCl added) with embedded 2.11 S/m annulus (blue) — scanned at 360 points; 0.11 S/m background with embedded 10.55 S/m annulus (blue) — scanned at both 360 and 720 points; and, 2.11 S/m background with embedded 10.55 S/m annulus (blue) — scanned only at 720 points. In addition to these scans, a "placebo" scan was also run, which just collects loss and position data in the absence of the phantom. From this scan, we were able to

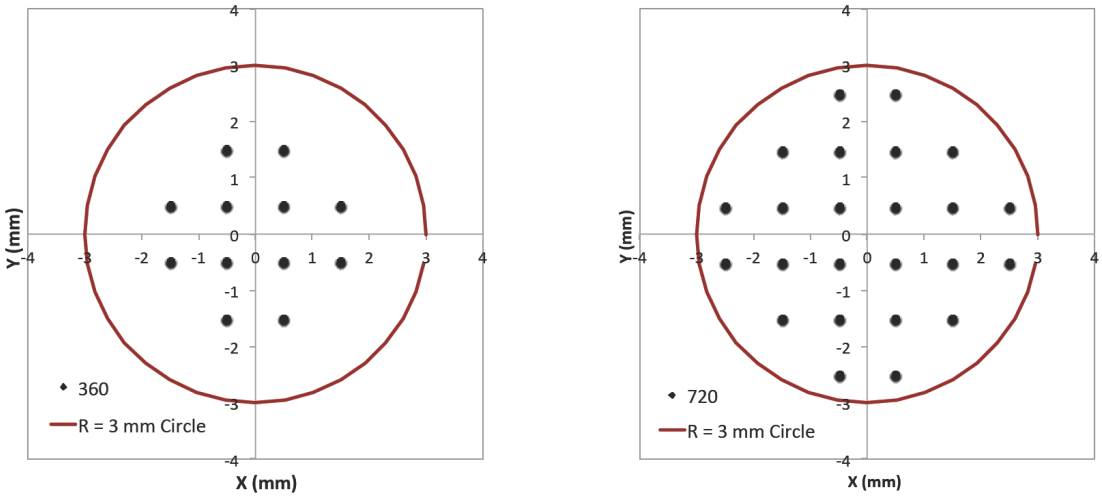

(a) (b)

Figure 3. (a) Shows 360 (12 × 30) sampling locations inside the 3.0 mm radius "sampling" disk — limits positioning of the coil's center, to avoid coil-phantom contact; (b) Shows 720 (24 × 30) sampling locations inside the same 3.0 mm radius "sampling" disk, for the sake of easy comparison.

determine that the error norm associated with inductive loss data is ∼ 0.03 ohms — due in part to noise, drift and interaction with nearby materials. Image reconstruction of acquired data involves the progressive reduction of the global regularization parameter τ until the solution error norm *approaches* 0.03 ohms from above. This involves setting τ to smaller singular values and observing the resultant error norm. For all scans, reduction of τ was discontinued at the tenth singular value, corresponding to error norms ranging from 0.04 to 0.05 ohms. Further reductions in error norm are not justified inasmuch as the noise floor of 0.03 ohms is approached too closely.

Arguably the easiest phantom to image is the one having the greatest contrast and highest conductivity inclusion — 10.55 S/m annular inclusion embedded in 0.11 S/m background. Two tomographic cuts are illustrated in Figures 4(a), (b) for the scan over 360 internal positions — one is normal to the X-axis while the other is normal to the Z-axis. Both are rotated to aid visualizing 3D structure while axes are shown to verify inclusion geometry, thickness and location.

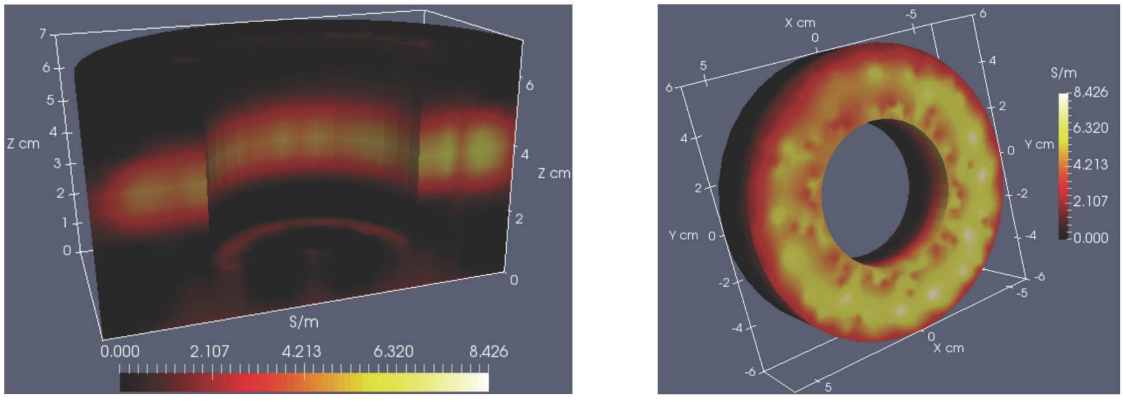

(a) (b)

Figure 4. (a) X-normal 3D cut of highest contrast phantom consisting of 10.55 S/m ring embedded in 0.11 S/m agarose — 360 scan positions; (b) Z-normal, 3D tilted cut of high contrast phantom scanned at 360 positions; attempt was made to cut through the annular inclusion at its midplane.

Figure 4(b) shows that reconstruction distributes conductivity nearly evenly across the annulus, moving in a radial direction, as it should. The reconstructed image for either Figure 4(a) or 4(b) shows that our phantom is not perfectly axisymmetric, but nevertheless close. Furthermore, the conductivity range falls short of the expected highest value of 10.55 S/m. Both observations are a result of our methods used to construct agarose phantoms, which involved successive layering of hot agarose. A first layer was poured and allowed to cool sufficiently to solidify, followed by pouring a subsequent layer of hot agarose which undoubtedly melts and stirs up a portion of the underlying material, causing some amount of asymmetry. Pouring the third layer is expected to further add to the problem. Since the conductivity of the inclusion falls well short of the intended 10.55 S/m, some amount of disturbance is suggested. Efforts were taken to minimize agarose layer melting by pouring successive layers only after agarose temperature had dropped to $\sim$ 10C above gelation temperature.

In an effort to more clearly discern the asymmetry observed in Figure 4(b), a second scan was done for the same phantom, with position and orientation left undisturbed, but using 720 scan points that covered more of the XY plane — more closely approaching the phantom wall should allow the "720 scan" to better resolve asymmetry. Image reconstruction results for the more extensive scan are shown in Figure 5, showing similar cuts and image orientations as in Figure 4, but with axes removed to reduce clutter.

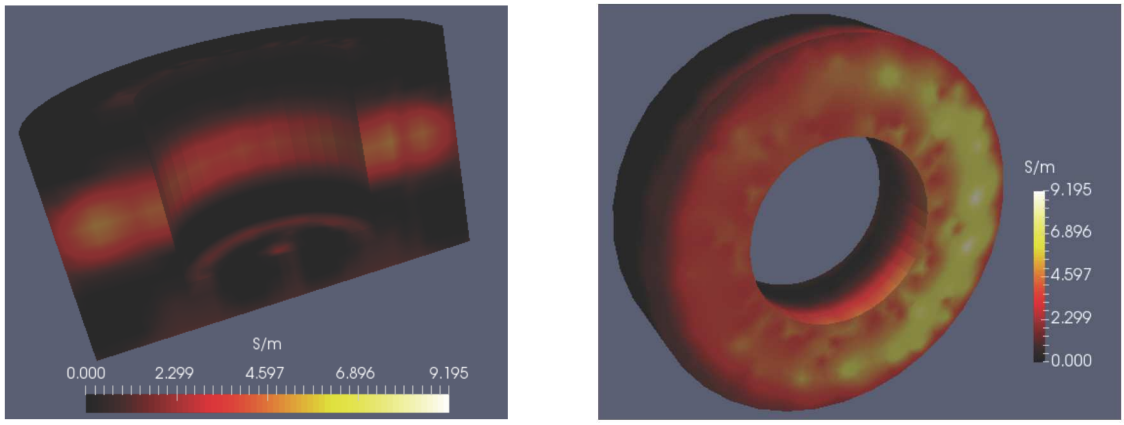

(a) (b)

Figure 5. (a) X-normal 3D cut of highest contrast phantom consisting of 10.55 S/m ring embedded in 0.11 S/m agarose — 720 scan positions; (b) Z-normal, 3D tilted cut of high contrast phantom scanned at 720 positions; attempt was made to cut through the annular inclusion at its mid-plane — orientation is nearly the same as in Figure 4(b).

As expected, Figure 5 also shows asymmetry, but more clearly than before. Since the conductivity of the inclusion still falls well short of the intended 10.55 S/m at most locations, some amount of disturbance is again suggested. Given that our method of phantom preparation introduces asymmetry through agarose remelting, then raising the background conductivity should yield a phantom having a reconstructed image showing an inclusion that more closely approaches 10.55 S/m. Thus, a phantom with background conductivity set at 2.11 S/m and inclusion set at 10.55 S/m as before was scanned at 720 locations — using the same scan points as for Figure 5. Furthermore, image reconstruction sets the global regularization parameter to the tenth singular value for both high and low background conductivity cases. Figure 6(a) shows a $Z_{\perp}$ cut through the middle of the inclusion alongside of an identical cut obtained for the phantom of Figure 5, which is shown in Figure 6(b). Both images show similar asymmetry, though rotated relative to each other. Since the image associated with the phantom having higher background conductivity shows higher conductivities by $\sim$ 1.5 S/m, we conclude that significant remelting does indeed occur and is unavoidable with our current technique.

Noise and drift in the current instrumentation are sufficiently low that imaging nearly axisymmetric phantoms with relatively high electrical conductivity is not too challenging. Our last phantom provides

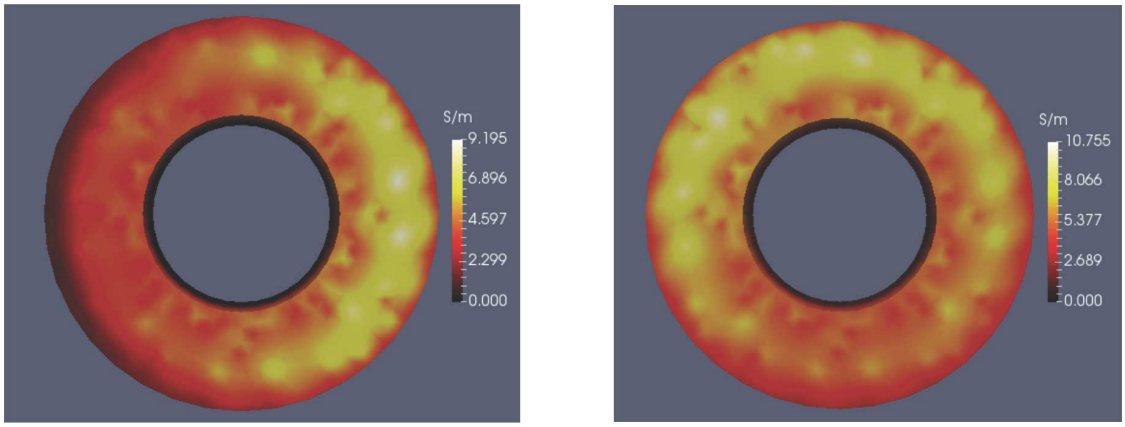

(a) (b)

Figure 6. (a) Z-normal cut through mid-plane of the 10.55 S/m inclusion embedded in 0.11 S/m agarose — 720 scan positions; (b) Z-normal cut through mid-plane of the 10.55 S/m inclusion embedded in 2.11 S/m agarose — 720 scan positions and identical orientation to cut in (a). In either case, views are in the $+Z$ direction, toward the 3-axis head.

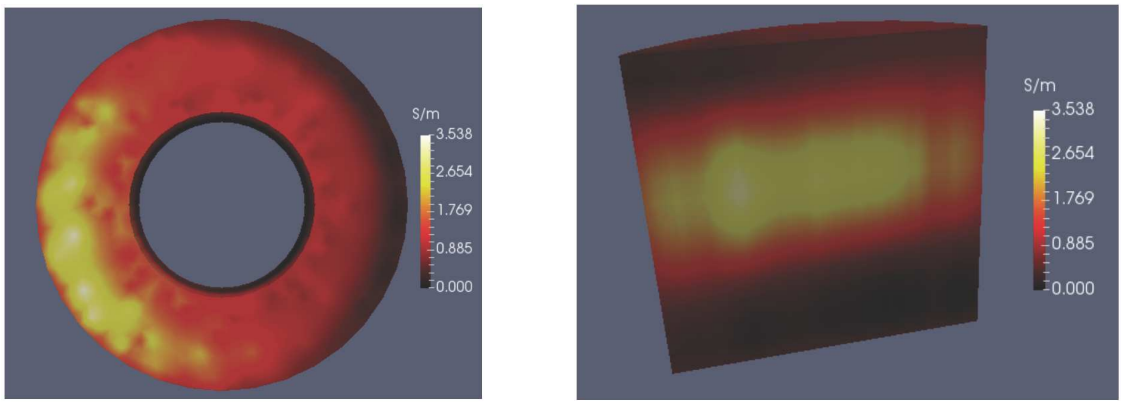

(a) (b)

Figure 7. (a) Z-normal cut through mid-plane of the 2.11 S/m inclusion embedded in 0.11 S/m agarose — 360 scan positions; (b) A cut passing through the wall where conductivity is highest — as observed in (a); the cut plane is parallel to the phantom's Z-axis and normal to the XY plane.

a greater challenge by reducing the conductivity of the embedded annular ring to 2.11 S/m and with matrix material set at 0.11 S/m. The results are shown in Figures 7(a) (b), with 7(b) providing an $XY_{\perp}$ cut directly through the most conductive zone found (mid-wall). Except for the cut shown in Figure 7(b), most of the embedded annulus shows an electrical conductivity beneath 2.11 S/m, suggesting as before that our phantoms experience some amount of layer remixing during construction. Nevertheless, conductivity observed in the cut of Figure 7(b) is well within the vicinity of the intended 2.11 S/m, which shows that images produced from an internal scan lead to reasonably correct conductivities directly from the convolution integral of Equation (1). The few points showing conductivity in far excess of 2.11 S/m are a consequence of numerical overshoot, a condition that becomes more common as lower conductivity systems are considered.

6. DISCUSSION OF RESULTS

Apart from geophysical applications, where 3D MIT has been proposed as a cross-well imaging strategy involving separate sources and detectors (e.g., Zhdanov and Yoshioka [8]), internal scans of low-conductivity objects via 3D MIT are not common, and perhaps non-existent for objects smaller than a few meters. Indeed, prior to the development and demonstration of single-coil MIT, imaging from internal electromagnetic scans of low-conductivity objects has not been reported in medical applications. But here, we have demonstrated on relatively small phantoms that maneuvering a single, small coil within the interior space of a conductive target while acquiring inductive loss and coil position data can be accomplished with sufficient accuracy to yield reasonable images after full 3D reconstruction. Since our 5.0 cm coil diameter is not much smaller than the inner diameter of the phantom's opening, the eddy currents induced by our single circular coil are expected to be nearly circular within the phantom body and nearly concentric to the phantom axis itself. This has the disadvantage of reducing sensitivity, since any flow of current through more highly conductive regions in heterogeneous media may also need to pass through regions of lower conductivity.

We attempted to reduce the challenges of heterogeneous media by working with nearly axisymmetric phantoms. But while building layered structures with molten agarose, whether doped with NaCl or not, we found there is some tendency for remelting of previously gelled material, sufficiently extensive to render the overall phantom non-axisymmetric. Furthermore, diffusion of Na^+ and Cl^- could also play a role in contributing to irregular conductivity boundaries and loss of axis-symmetry. In one instance, we assessed the effects of remixing by using 2.11 S/m agarose as background for a 10.55 S/m inclusion, and then noting inclusion conductivity in the reconstructed image. In this case, inclusion conductivity more closely followed expectations than when 0.11 S/m agarose was used as background, confirming the impact of remelting and possibly diffusion. Future work will include the design and creation of phantoms that reduce the effects of melting and diffusion.

Nevertheless, our image reconstruction algorithm successfully provided conductivity values well within the vicinity of what was expected and correct inclusion dimensions. Furthermore, the use of depth-dependent regularization did an excellent job of balancing out the inherent bias of the convolution integral kernel and yielded images showing a conductivity that is for the most part smooth and unchanging in the radial direction — exactly what should be expected for these nearly axisymmetric phantoms. A key conclusion reached from this observation is that internal scans using single-coil MIT can be expected to image structure at depths up to 3.0 cm — the thickness of our phantom's wall. This distance places a number of biologically interesting structures within the realm of single-coil internal imaging, such as the intestine, esophagus, trachea, urethra and vagina.

Practical image reconstruction using the single-coil approach, whether from internal or external scans, will require improvements in electronics. Noise, drift and unwanted coupling effects (e.g., with 3-axis controller) need to be reduced sufficiently, so that inductive loss error norms are correspondingly reduced as much as 10× from the current value of ~ 0.03 ohm. Low error norms are required in order to cope with strongly heterogeneous materials that may consist of smaller, isolated high conductivity inclusions fully embedded in very low conductivity matrix material [25]. And if internal scans are to be useful in biological applications, sensor size must also be reduced. In an extreme case, sensor (coil) size would need to be reduced to about 5.0 mm diameter in order to perform an internal imaging scan along the length of the urethra, with a goal of imaging the prostate. The smallest coil diameter we have worked with to date is 24 mm [14], which is small enough for a rectal or esophageal scan, but not the urethra. We believe further size reductions are achievable goals, given current industry emphasis on delivering inductive-to-digital converters in small integrated circuit packages (3 mm × 3 mm × 1 mm) at economical cost. However, the fact that *single-coil* MIT is, for the first time, able to reconstruct the conductivity distribution of a conductive feature embedded in a small phantom via "internal scanning" indicates that this new scanning modality holds promise, while greatly extending the usefulness of the technique.

APPENDIX A. RING FUNCTION

A suitable definition for the ring function, first presented in Section 2, is given as an integral formula by Gradshteyn and Ryzhik [20] on page 1001:

$$Q_{1/2}(\eta) = \frac{1}{\sqrt{2}} \int_0^\pi \frac{\cos(t)dt}{\sqrt{\eta - \cos(t)}} \tag{A1}$$

Rather than work from Equation (A1), a hypergeometric form of Equation (A1) was found to be much more efficient for computational work and is found on page 1022 of the same reference.

REFERENCES

1. Borcea, L., "Electrical impedance tomography," *Inverse Problems*, Vol. 18, R99–R136, 2002.
2. Sikora, J., *Boundary Element Method for Impedance and Optical Tomography*, Oficyna Wydawnicza Politechniki Warszawskiej, ISBN: 978-83-7207-728-8, 2007.
3. Sikora, J. and S. Wòjtowicz, eds., *Industrial and Biological Tomography: Theoretical Basis and Applications*, Wydawnictwo Książkowe Instytutu Elektrotechniki, ISBN: 978-83-61956-04-4, 2010.
4. Wei, H. Y. and M. Soleimani, "Electromagnetic tomography for medical and industrial applications: Challenges and opportunities," *Proc. IEEE*, Vol. 101, 559–564, 2013.
5. Stawicki, K. and S. Gratkowski, "Optimization of signal coils in the magnetic induction tomography system," *Przeglad Elektrotechniczny*, Vol. 86, No. 5, 74–77, 2010.
6. Zakaria, Z., et al., "Advancements in transmitters and sensors for biological tissue imaging in magnetic induction tomography," *Sensors*, Vol. 12, 7126–7156, 2012.
7. Al-Zeibak, S. and H. N. Saunders, "A feasibility study of in vivo electromagnetic imaging," *Physics in Medicine and Biology*, Vol. 38, No. 1, 151–160, 1993.
8. Zhdanov, M. S. and K. Yoshioka, "Cross-well electromagnetic imaging in three dimensions," *Exploration Geophysics*, Vol. 34, 34–40, 2003.
9. Ma, L., H.-Y. Wei, and M. Soleimani, "Planar magnetic induction tomography for 3D near subsurface imaging," *Progress In Electromagnetic Research*, Vol. 138, 65–82, 2013.
10. Scharfetter, H., K. Hollaus, J. Rosell-Ferrer, and R. Merwa, "Single-step 3D image reconstruction in magnetic induction tomography: Theoretical limits of spatial resolution and contrast to noise ratio," *Annals of Biomedical Engineering*, Vol. 34, No. 11, 1786–1798, 2006.
11. Dekdouk, B., C. Ktistis, D. W. Armitage, and A. J. Peyton, "Absolute imaging of low conductivity material distributions using nonlinear reconstruction methods in magnetic induction tomography," *Progress In Electromagnetic Research*, Vol. 155, 1–18, 2016.
12. Feldkamp, J. R., "Single-coil magnetic induction tomographic three-dimensional imaging," *J. Medical Imaging*, Vol. 2, No. 1, 013502, 2015.
13. Feldkamp, J. R. and S. Quirk, "Validation of a convolution integral for conductivity imaging," *Progress in Electromagnetic Research Letters*, Vol. 67, 1–6, 2017.
14. Feldkamp, J. R. and S. Quirk, "Coil geometry effects on single-coil magnetic induction tomography," *Physics in Medicine and Biology*, Vol. 62, 7097–7113, May 2017.
15. Joines, M. T., Y. Zhang, C. Li, and R. L. Jirtle, "The measured electrical properties of normal and malignant human tissues from 50 to 900 MHz," *Medical Physics*, Vol. 21, No. 4, 547–550, 1994.
16. Sudduth, K. A., N. R. Kitchen, W. J. Wiebold, W. D. Batchelor, G. A. Bolero, D. E. Clay, H. L. Palm, F. J. Pierce, R. T. Schuler, and K. D. Thelen, "Relating apparent electrical conductivity to soil properties across the north-central U.S.A," *Computers and Electronics in Agriculture*, Vol. 46, 263–283, 2005.
17. Palacky, G. J., "Resistivity characteristics of geologic targets (ch. 3)," *Electromagnetic Methods in Applied Geophysics*, Vol. 1, 53–129, 1988.
18. Feldkamp, J. R., "Inversion of an Inductive Loss Convolution Integral for Conductivity Imaging," *Progress In Electromagnetic Research B*, Vol. 74, 93–107, 2017.

19. Parise, M., "On the surface fields of a small circular loop antenna placed on plane stratified earth," *Intl. J. of Antennas and Propagation*, Vol. 2015, Article ID 187806, 8 pages, http://dx.doi.org/10.1155/2015/187806, 2015.
20. Gradshteyn, I. S. and Ryzhik, *Table of Integrals, Series and Products*, Corrected and Enlarged Edition, A. Jeffrey, Academic Press, New York, NY, 1980.
21. Lapidus, L. and G. F. Pinder, *Numerical Solution of Partial Differential Equations in Science and Engineering*, Wiley-Interscience, J. Wiley & Sons, NY, 1982.
22. Eldén, L., "Algorithms for the regularization of ill-conditioned least squares problems," *BIT*, Vol. 17, 134–145, 1977.
23. Donatelli, M., A. Neuman, and L. Reichel, "Square regularization matrices for large linear discrete ill-posed problems," *Numerical Linear Algebra with Applications*, Vol. 19, 896–913, 2012.
24. Katamreddy, S. H. and P. K. Yalavarthy, "Model-resolution based regularization improves near infrared diffuse optical tomography," *J. Opt. Soc. Am.*, Vol. 29, No. 5, 649–656, 2012.
25. Feldkamp, J. R. and S. Quirk, "Effects of tissue heterogeneity on single-coil, scanning MIT imaging," *Proc. SPIE 9783, Medical Imaging: Physics of Medical Imaging*, 978359, 2016.
26. Feldkamp, J. R. and S. Quirk, "Optically tracked, single-coil, scanning magnetic induction tomography," *J. Medical Imaging*, Vol. 4, No. 2, 023504, 2017.
27. Feldkamp, J. R. and S. Quirk, "Optically tracked, single-coil, scanning magnetic induction tomography," *Proc. SPIE 10132, Medical Imaging: Physics of Medical Imaging*, 10132172, 2017.